minerals

MDPI

Article

Rare Earth Element Fluorocarbonate Minerals from the Olympic Dam Cu-U-Au-Ag Deposit, South Australia

Danielle S. Schmandt [1,*], Nigel J. Cook [1], Cristiana L. Ciobanu [1], Kathy Ehrig [2], Benjamin P. Wade [3], Sarah Gilbert [3] and Vadim S. Kamenetsky [4]

1 School of Chemical Engineering, The University of Adelaide, Adelaide, SA 5005, Australia; nigel.cook@adelaide.edu.au (N.J.C.); cristiana.ciobanu@adelaide.edu.au (C.L.C.)
2 BHP Olympic Dam, Adelaide, SA 5000, Australia; kathy.ehrig@bhpbilliton.com
3 Adelaide Microscopy, The University of Adelaide, Adelaide, SA 5005, Australia; benjamin.wade@adelaide.edu.au (B.P.W.); sarah.gilbert@adelaide.edu.au (S.G.)
4 School of Physical Sciences, University of Tasmania, Hobart, TAS 7001, Australia; dima.kamenetsky@utas.edu.au
* Correspondence: danielle.schmandt@adelaide.edu.au; Tel.: +61-472-665-835

Received: 31 August 2017; Accepted: 17 October 2017; Published: 23 October 2017

Abstract: Olympic Dam is a world-class breccia-hosted iron-oxide copper-gold-uranium ore deposit located in the Gawler Craton, South Australia. It contains elevated concentrations of rare earth elements (REE) which occur as the REE minerals bastnäsite, synchysite, florencite, monazite, and xenotime. This is the first study to focus on the mineralogy and composition of the most abundant REE mineral at Olympic Dam, bastnäsite, and subordinate synchysite. The sample suite extends across the deposit and represents different sulfide mineralization styles (chalcopyrite-bornite and bornite-chalcocite) and breccias of various types, ranging from those dominated by clasts of granite, dykes, and hematite. The REE-fluorocarbonates (bastnäsite and synchysite) typically occur as fine-grained (<50 μm) disseminations in Cu-Fe-sulfides and gangue minerals, and also within breccia matrix. They are also locally concentrated within macroscopic REE-mineral-rich pockets at various locations across the deposit. Such coarse-grained samples formed the primary target of this study. Three general textural groups of bastnäsite are recognized: matrix (further divided into disseminated, fine-grained, and stubby types), irregular (sulfide-associated), and clast replacement. Textures are largely driven by the specific location and prevailing mineral assemblage, with morphology and grain size often controlled by the associated minerals (hematite, sulfides). Major element concentration data reveal limited compositional variation among the REE-fluorocarbonates; all are Ce-dominant. Subtle compositional differences among REE-fluorocarbonates define a spectrum from relatively La-enriched to (Ce + Nd)-enriched phases. Granite-derived hydrothermal fluids were the likely source of F in the REE-fluorocarbonates, as well as some of the CO_2, which may also have been contributed by associated mafic-ultramafic magmatism. However, transport of REE by Cl-ligands is the most likely scenario. Stubby bastnäsite and synchysite may have formed earlier, coincident with hydrothermal alteration of granite releasing Ca from feldspars. Other categories of bastnäsite, notably those co-existing with sulfides, and reaching the top of the IOCG mineralization at Olympic Dam (chalcocite + bornite zone) are relatively younger. Such an interpretation is concordant with subtle changes in the REE patterns for the different categories. The common association of bastnäsite and fluorite throughout the deposit is typical of the hematite breccias and can be deposited from neutral, slightly acidic fluids (sericite stability) at T ≈ 300 °C.

Keywords: Olympic Dam; bastnäsite; synchysite; mineral compositions

1. Introduction

The >10,000 million ton Olympic Dam Cu-U-Au-Ag deposit [1] is the largest iron oxide copper gold (IOCG)-type deposit in the world, and by far the largest of several deposits and smaller prospects within the Gawler Craton. Rare earth elements (REE) are prominent components of many IOCG systems (e.g., [2,3]). Approximate concentrations of the light REE (LREE) and heavy REE plus yttrium (HREE + Y) within the Olympic Dam total resource are 3053 ppm and 110 ppm, respectively. The deposit thus represents a global-scale anomaly with respect to REE. Despite this considerable endowment, no REE are currently recovered at Olympic Dam, or elsewhere in the Olympic Cu Province. This is primarily due to relatively low REE grades, small grain size of host minerals, their dissemination throughout the deposit, and the dominance of LREE over the more economically attractive HREE. Nevertheless, the distribution and mineralogy of REE in the deposit are of major interest and potentially significant for reconstructing ore genesis and regional-scale exploration with respect to potential future exploitation.

The fluorocarbonate bastnäsite [$REE(CO_3)F$] and florencite [$REEAl_3(PO_4)_2(OH)_6$] form the two most prominent REE-minerals at Olympic Dam. They were first identified and described by Roberts and Hudson [4], who noted the good correlation between concentrations of REE and Fe, Cu, Au, U, and F. Oreskes and Einaudi [5] highlighted REE enrichment at Olympic Dam and included brief descriptions of four major REE-minerals (bastnäsite, florencite, monazite, and xenotime), on which Lottermoser [6] provided additional description. The most recent review of the Olympic Dam deposit [7] refers to an additional REE-fluorocarbonate, synchysite [$CaREE(CO_3)_2F$], as well as REE-Al-bearing phosphate-sulphates of the beudantite group. There has, however, been no prior systematic study of REE-minerals from Olympic Dam, with respect to either petrography, relationships with other minerals, or with respect to chemical composition and variation. This is despite much recent work providing detailed description of other REE-carriers at Olympic Dam, including the U-minerals (uraninite, brannerite, and coffinite) [8,9], apatite [10,11], and feldspars [12,13]. These contributions have helped understand REE distributions at the deposit-scale, and allowed insights into deposit formation.

In this contribution, we address the petrography and chemical composition of the REE-fluorocarbonates, bastnäsite and synchysite, from the Olympic Dam orebody. Bastnäsite is by far the most abundant discrete REE-mineral, and is found throughout the orebody. We have aimed at describing the occurrence of bastnäsite and subordinate synchysite, including samples containing anomalously high REE concentrations and/or macroscopic REE-minerals. Petrographic description is followed by analysis of their compositions, in terms of both major oxides and trace elements. The results permit an evaluation of the occurrence of the dominant REE-minerals at Olympic Dam, as well as insights into the geochemical behavior of REE and the potential source(s) of these elements.

2. Background

2.1. REE-Fluorocarbonate Minerals

Rare earth element fluorocarbonates of the bastnäsite-synchysite group (BSG) are defined as mixed-layer compounds with hexagonal and rhombohedral symmetry in which REE- and Ca-bearing layers with various stacking arrangements can adapt to any intermediate composition between the end-members bastnäsite [$REE(CO_3)F$; *B*-slab] and synchysite [$CaREE(CO_3)_2F$; *S*-slab] [14–16]. However, there are only two other named minerals within the group: parisite (*BS*); and röntgenite (BS_2), as well as a handful of B_nS_m polytypes (*n*, *m*-number of *B* and *S* slabs, respectively) defined only as long-range stacking sequences (observed over hundreds of nm), e.g., B_2S, based on TEM investigations, e.g., [15,17,18]. Monoclinic symmetry is considered for parisite and synchysite based upon refinement of single crystal studies [19,20]. The stability of such mixed-layer compounds is useful for tracking the thermodynamic conditions of ore deposition [21,22].

The recognition of the low-temperature hydroxyl-bastnäsite group indicates that bastnäsite can accommodate some OH in place of F, before altering structurally [23]. The completeness of

solid solution and the stability of bastnäsite with intermediate OH–F composition are, however, questionable [24,25]. A further group is the REE-oxyfluorides (e.g., haleniusite [REEOF]) that may form at high-temperature as a breakdown product of bastnäsite [22,26].

The REE-fluorocarbonates are typically LREE-enriched and the dominant minerals making up global LREE reserves, e.g., [22].

2.2. Olympic Dam Mineralogy

The Olympic Dam deposit is located 520 km NNW of Adelaide, South Australia, on the Western Gawler Craton. The Olympic Dam deposit is contained completely within the Olympic Dam Breccia Complex (ODBC; Figure 1), hosted in the Roxby Downs Granite (RDG) within the greater Gawler silicic large igneous province (SLIP; [27]). The main mineralizing event is interpreted to have taken place at ~1590 Ma [28–31], coincident with RDG emplacement.

The geological setting and mineralogy of the Olympic Dam deposit have been described in detail elsewhere, e.g., [7]. The dominant minerals in the ODBC are hematite, quartz, sericite, feldspars, barite, fluorite, siderite, chlorite, pyrite, chalcopyrite, bornite, and chalcocite. The REE-minerals make up a total of ~0.18 wt % of the deposit: bastnäsite (~0.0833%), florencite (~0.066%), monazite (~0.0184%), synchysite (~0.0124%), and xenotime (~0.0045%) from modal mineralogy based on a 10,000 sample Mineral Liberation Analysis (MLA) dataset [7]. Along with the discrete REE-minerals, REEs are also present in solid solution within various abundant common minerals, including apatite, brannerite, coffinite, uraninite, thorite, *uranothorite*, and zircon [7,8,10].

The concentration of many elements, including REE, correlates with total whole-rock Fe concentration across the deposit [7]. The abundance of REE is broadly coincident with copper sulfide mineralization, and correlates positively with Fe wt %, increasing towards the center, although depleted in the Fe-dominant, sulfide-poor deposit core. REE-minerals and Cu-(Fe)-sulfides are often associated with one another on the scale of individual polished sections [5,7].

The two primary REE-fluorocarbonates at Olympic Dam are bastnäsite and synchysite. Bastnäsite accounts for 2.5% of all carbonates, while synchysite represents 0.4%. The other carbonates are siderite, ankerite, and dolomite-calcite, in order of decreasing abundance [7,32]. Two other REE-fluorocarbonates, parisite and an unnamed compound *B2S* (these have Ca content lying intermediate between bastnäsite and synchysite), have been identified distal to the deposit within the RDG [13,33].

3. Sampling and Analytical Methods

3.1. Sampling

The sample suite analyzed here includes 20 specimens collected from diamond drill core located across the orebody (Table 1, Figure 1) and were originally collected as part of an earlier project [34] to characterize the REE minerals. Samples were identified, and subsequently sampled, by querying the BHP Olympic Dam drill core assay database for anomalously high REE drill core intersections (see [7]). While anomalous, they are invaluable for this study of REE mineralogy as the majority of REE-minerals are typically fine-grained and disseminated throughout the deposit and often intergrown with other minerals making microanalysis difficult. X-ray diffraction (XRD) was carried out by CSIRO (in Adelaide) on each of the high-REE drill core intervals to determine the major mineral composition (Supplementary Table S1). Each sample was mounted in epoxy as a one-inch diameter polished block.

The samples were taken from lithologies logged as: (1) breccias containing dyke clasts; (2) granite-rich breccias; (3) hematite-rich breccia; and (4) sericitized dyke (Table 1). The "breccias containing dyke clasts" are zones of breccias with associated undifferentiated mafic dyke clasts; these breccias have a recognizable mafic component which has survived alteration. Such breccias occur across the deposit, with the sample suite including representative examples from the NW arm, central, and eastern edge of the deposit. The "granite-rich breccias" are breccia zones dominated by granite breccia clasts which occur across the deposit; samples include examples from the NW arm, central, and eastern edge

of the deposit. The "hematite-rich breccias" contain abundant hematite as both clasts and matrix. The samples of this lithology are derived from the center and eastern edge of the deposit. Sericitized dykes are recognized as paragenetically early within the deposit and are highly altered; the dyke sampled in this study is located towards the far NW edge of the resource.

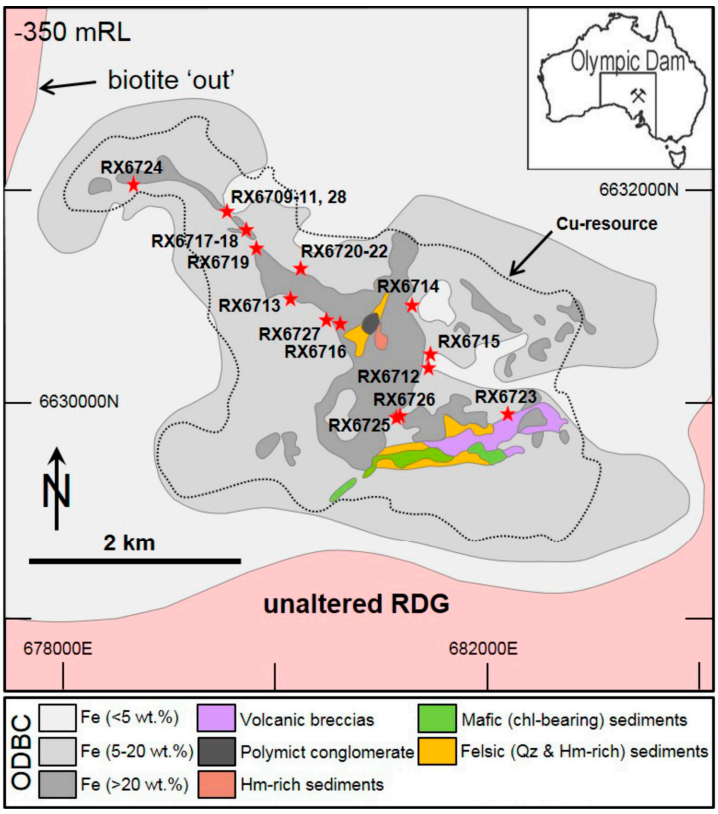

Figure 1. Sketch map of Olympic Dam orebody (−350 mRL) showing sample locations.

3.2. Analytical Methods

All microanalytical work was undertaken at Adelaide Microscopy, The University of Adelaide. Each polished block was examined and imaged using a reflected light optical microscope and using a FEI Quanta 450 Field Emission Gun (FEG) scanning electron microscope (SEM) (FEI, Eindhoven, The Netherlands) equipped with a silicon-drift detector energy-dispersive X-ray (EDAX) spectrometer. Quantitative compositional element data were acquired using a Cameca SX-Five electron probe microanalyzer (EPMA) (Cameca, Paris, France), supplemented with trace element determinations by laser ablation inductively coupled plasma mass spectrometry (LA-ICP-MS) (RESOlution-LR ArF excimer laser ablation system, Australian Scientific Instruments, Canberra, Australia, coupled to an Agilent 7700x Quadrupole ICP mass spectrometer; Agilent Technologies, Santa Clara, CA, USA). The latter method proved valuable to obtain quantitative concentration data for elements present in low abundance, including heavy REE, U, Th, and Pb. Full details on the two analytical methods can be found in Supplementary Material 1, Tables S2 and S3 (EPMA), and Supplementary Material 2 and Table S4 (LA-ICP-MS).

Table 1. Summary description and mineralogy of samples discussed in this study.

Lithology	Sample Location				Brief Sample Description [1]	REE Fluorocarbonate Occurances					
						Bastnasite					Synch-Ysite
						Matrix			Irregular Sulfide Associated	Clast Replace-Ment	
	Area	Drill Hole	Sample No.	Core Depth (m)		Stubby	Cement	Dissem-Inated			
Breccias containing dyke clasts	NW arm	RU34-3829	RX6709	72.8–73.0	Strong Bst matrix zone with clasts of Ser and Chl. Around Bst zones are Hm dominate zones with Hm as matrix and clasts with Ser-Chl. Rt and Zr present.	X					
			RX6710	73.6–73.7	Hm is the major mineral, present in clasts and with strong lineaments in matrix. Distinct zones with abundant angular-rounded clasts of Ser-Chl. Zr present.	X					
			RX6711	74.7–74.8	Strong foliation across the sample. More fine-grained sample of mostly Ser with Chl, few and small clasts, mostly composed of Hm. Flo occurs along "pressure shadows" around mineral grains. Rt and Zr present.			X			
		RU41-2571	RX6728	174.8–174.9	Mostly Hm with "crackle" Bar veinlets with Bst around clasts and Hm. Some clasts of Hm, Qz, and Ser.	X					
	East edge	RU33-159	RX6714	66.3–66.4	Sample dominated by Hm as clasts and matrix with Ser. Hm makes rounded thick rims around cores of Ser and Bar. Bst concentrated in light-colored zone on edge.			x		X	X
		RU37-7354	RX6723	4.3–4.4	Bst occurs as blades in the matrix, both disseminated and abundant in distinct zones, and in relict clasts. Abundant clasts of mostly Qz in sample, rounded-angular, all sizes. Orange areas on hand sample are mostly Qz + Hm.			x		X	
	Central	RU34-454	RX6716	82.9–83.0	Very abundant Bst throughout sample, concentrated in more fine-grained conduit, as matrix and clast replacement. Around Bst zone is mostly Hm as clasts and matrix.		X			x	
		RU45-2661	RX6727	51.8–51.9	Chaotic sample with blocky zones of fine grained Ser and Hm matrix. Other areas of breccia conduits with abundant clasts of Qz, Hm, sulfides, and Bar.		X			x	
Granite-rich breccias	East edge	RU3-558	RX6712	23.7–23.8	Clasts are mostly Qz with some Bar and Hm, rounded to angular. Ser matrix. Rt and Zr present.			x			
		RU4-105	RX6715	12.2–12.3	Abundant clasts, rounded to angular, matrix supported heterolithic breccia but clasts mostly of Qz and Hm, matrix is microbreccia and Ser.			x			
	Central	RU3-954	RX6713	70.1–70.2	Hm abundant as matrix and clasts. Other clats of sulfide, Qz, and Ser. Bn vein. Lacking pervasive disseminated bast in the matrix, Flo is present instead. Rt present.					X	

Table 1. *Cont.*

Lithology	Sample Location				Brief Sample Description [1]	REE Fluorocarbonate Occurances					
						Bastnasite					Synch-Ysite
						Matrix			Irregular Sulfide Associated	Clast Replace-Ment	
	Area	Drill Hole	Sample No.	Core Depth (m)		Stubby	Cement	Dissem-Inated			
Granite-rich breccias	NW arm	RU31-751	RX6717	90.3–90.4	Large cross cutting vein of Fl Abundant Qz clasts of ranging size, rounded to angular. Bst in matrix concentrated in localized zones, otherwise Ser and Hm. Rt and Zr present.		X	x			
			RX6718	90.8–91.0	Similar to above. Bst mostly occurs as fine-grained blades concentrated in zones as the matrix. More abundant irregular Bst "clumps". Zr and Rt present.		X	x			
		RU31-767	RX6719	5.3–5.4	Zone of Qz clasts with strong veinlet features. Other zone dominated by Hm with less defined directional features. Fine grained blade Bst as matrix around fine-grained rounded Qz clasts.		X	x			
Hematite-rich breccia	Central	RU40-1407	RX6720	19.0–19.2	Primarily composed of coarse-grained Hm with a range of textures. Cluster of clasts of rounded to angular Fl and minor Qz and Cp/Bn. Bst matrix in distinct veinlet zone with Cp and Bn.				X		
			RX6721	19.4–19.5	Strong linear zones from veins of Hm and Ser with Cp-Bn between bands of Fl clasts with matrix of Ser, Hm, Bst, and Cp-Bn.				X		
			RX6722	19.7–19.8	Matrix supported; abundant clasts, rounded to angular, composed primarily of either Fl, Qz, and Cu-(Fe) sulfides in matrix of blade Hm. Rare irregular Bst. Fl clasts are the largest.				X		
	East edge	RU38-2994	RX6725	92.8–92.9	Heterolithic clasts and clasts of mostly Qz and Hm in microbreccia of mostly Ser with also fine-grained bladed Hm and Bst.		x	X			
		RU38-2685	RX6726	77.1–77.3	Clasts of mostly Qz, Ser, Hm, and Bst. Microbreccia matrix of fine-grained Hm blades and Ser with veinlets and lineation around clasts. Rt and Zr are present.			x		X	X
Sericitized dyke	NW arm	RU41-5181	RX6724	183.7–183.8	Bst in distinct zones in darker red areas. Fine grained Bst in matrix to massive clumps. Clumps are dirty with possible faint zoning from inclusions of Hm and Ser but mostly irregular. Some distinct zones of Flo with distinct hexagonal textures with Ser in shape. Fine grained irregular Bst in Ser around Flo.		X	x			

[1] Mineral abbreviations: Hm—hematite; Qz—quartz; Chl—chlorite; Fl—fluorite; Bar—barite; Flo—florencite; Bst—bastnäsite; Ser—sericite; Cp—chalcopyrite; Bn—bornite; Cc—chalcocite; Rt—rutile; Zr—zircon. XRD analysis of major minerals of sample areas are included in Supplementary Table S1. X—major, x—minor.

4. Petrography

The occurrence of discrete REE-minerals at Olympic Dam is extremely varied but they can be generally typified as fine-grained (<50 μm), and occurring as disseminations with sulfide and gangue minerals throughout all ore zones in the deposit. They can, however, also be locally concentrated to macroscopic REE-mineral rich pockets which are described in detail here.

The various lithologies represented in this study display mineralogical and textural differences across the sample set (Table 1, Supplementary Figure S1). "Breccias containing dyke clasts" are generally hematite–sericite dominant with variable to high abundance of quartz or bastnäsite, and can also contain florencite. The sulfide assemblage in these samples mostly comprises bornite and chalcocite. "Granite-rich breccias" can be recognized from their color and bulk composition and typically contain trace amounts of Cu-(Fe)-sulfides (chiefly bornite and chalcocite). Florencite is a minor but persistent component of these samples. The "hematite-rich breccia" is represented by two domain types, one dominated by hematite and fluorite; the second domain contains no fluorite but more abundant quartz and sericite with hematite. Fluorite occurs either as clasts, agglomerated or evenly distributed, or as veinlets (Supplementary Figure S1) within the hematite-sericite matrix. Bastnäsite and sulfides (chalcopyrite-bornite) are present in variable amounts within both domains. The sericitized dyke sample is aptly named as it comprises ~78% sericite with abundant bastnäsite and some hematite, minor florencite, but no Cu-(Fe)-sulfides. All samples contain minor amounts of uranium minerals (uraninite and subordinate brannerite and coffinite) and a variety of other accessories, including cobaltite (CoAsS), altaite (PbTe), hessite (Ag_2Te), löllingite ($FeAs_2$), native copper, and gold (electrum).

4.1. Bastnäsite

In these samples bastnäsite occurs in three main forms: within the matrix, as irregular grains associated with sulfides, and replacing breccia clasts (Figures 2–5).

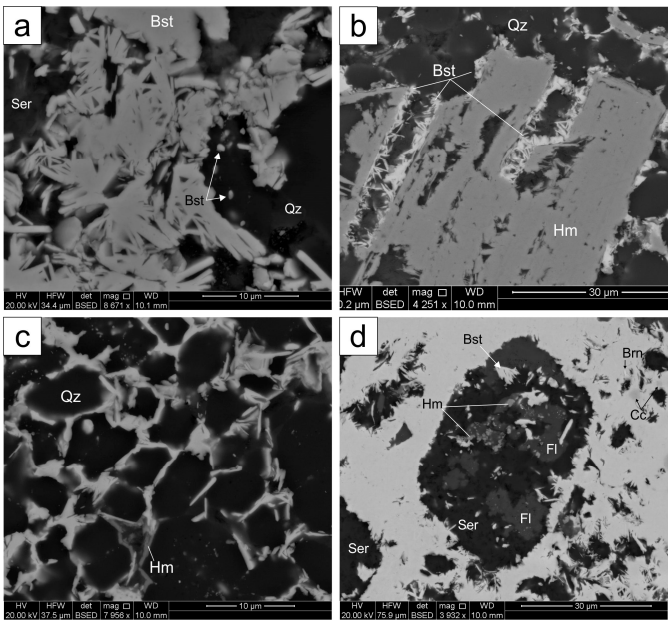

Figure 2. Backscatter electron (BSE) images showing textural aspects of fine-grained matrix bastnäsite: (**a**) Fine-grained bladed matrix bastnäsite (Bst) concentrated along boundaries of other gangue minerals (quartz-Qz, sericite-Ser) in the breccia matrix (sample RX6717); (**b**) Platy bastnäsite on hematite (Hm) and interstitial between quartz (sample RX6719); (**c**) Detail of (**b**) showing fine-grained bladed bastnäsite (white) interstitial to quartz with hematite; (**d**) Aggregated fine-grained matrix bastnäsite as a cement for other minerals (fluorite-Fl, hematite, sericite) within the breccia. Minor brannerite (Brn) and chalcocite (Cc) are enclosed by bastnäsite cement (sample RX6719).

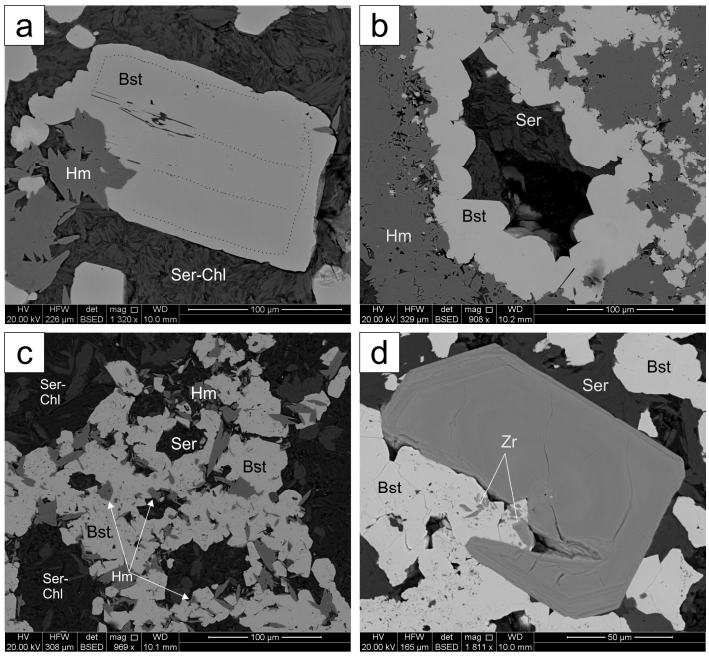

Figure 3. BSE images showing textural aspects of stubby matrix bastnäsite: (**a**) Individual stubby bastnäsite (Bst). Black line outlines pattern of hematite (Hm) and sericite (Ser) inclusions (sample RX6728). Chl-chlorite; (**b**) Stubby bastnäsite along margins of cavity with open space filled by sericite (sample RX6728); (**c**) Stubby bastnäsite forming a cement to other matrix minerals (sample RX6710); (**d**) Zircon (Zr) enclosed and partially replaced by bastnäsite cement (sample RX6709).

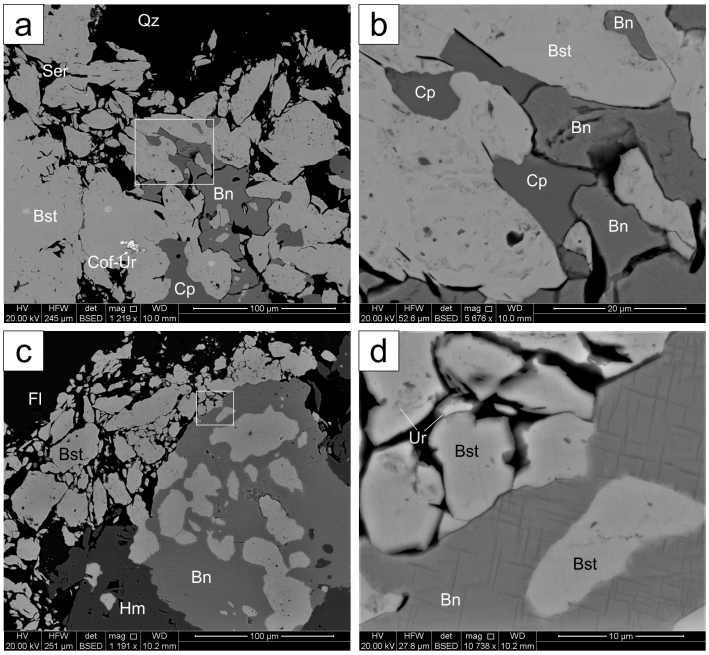

Figure 4. BSE images showing textural aspects of sulfide-associated bastnäsite: (**a**) Bastnäsite (Bst) with interstitial chalcopyrite (Cp) and bornite (Bn). Note scalloped boundaries between sulfides and bastnäsite (sample RX6720). Cof-Ur: uraninite with rim of coffinite, Qz-quartz, Ser-sericite; (**b**) Detail of domain shown by white box on (**a**). Discolorations in bastnäsite are fine inclusions of hematite and sericite; (**c**) Patchy, subhedral bastnäsite in matrix and within bornite (Sample RX6721). Fl-fluorite, Hm-hematite; (**d**) Detail of domain shown by white box on (**c**). Bornite displays lamellar exsolution of chalcopyrite. Uraninite is included in, and interstitial to bastnäsite.

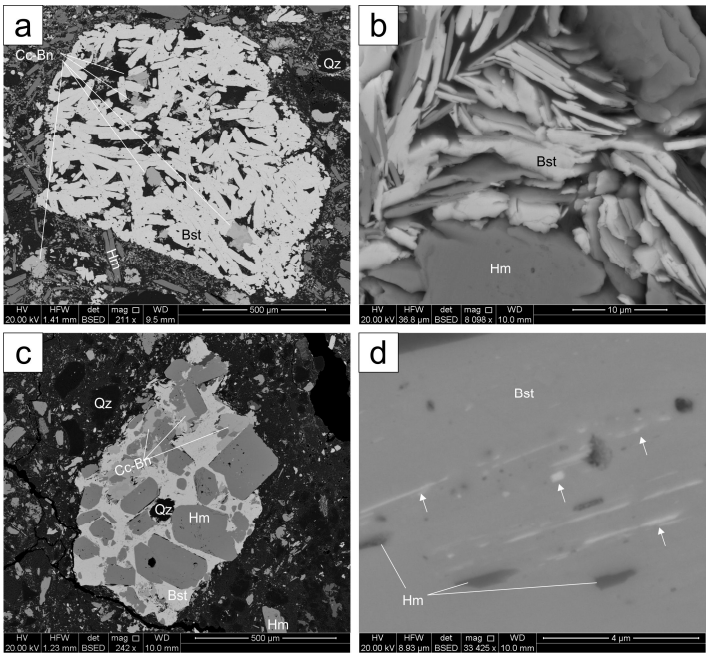

Figure 5. BSE images showing petrographic aspects of clast replacement bastnäsite: (**a**) Bladed aggregates of bastnäsite psuedomorphing the outline of a replaced clast (sample RX6726). Qz-quartz, Cc-chalcocite, Bn-bornite, Hm-hematite; (**b**) Feather-like bastnäsite with hematite (sample RX6713); (**c**) Bastnäsite forming a cement around hematite within breccia clast (sample RX6723); (**d**) Coarse-grained bastnäsite with hematite inclusions; arrows indicate brighter bands, which may be richer in HREE or contain more F and less CO_3 (sample RX6714).

4.1.1. Matrix Bastnäsite

Bastnäsite in the matrix is the most varied of the bastnäsite occurrences in terms of grain size, abundance, and morphology. Breccias with matrix bastnäsite can be either clast- or matrix-supported. The appearance of both types and bastnäsite growth patterns are suggestive of high transient porosity, which is preserved in some domains. The most common and pervasive form of bastnäsite across the entire deposit is fine-grained (1–50 μm-sized) disseminations with morphologies ranging from blades to laths and irregular grains. Although pervasively distributed throughout the breccia matrix, bastnäsite may reach high abundance in the matrix within restricted breccia domains. For example, aggregates of bladed bastnäsite are locally concentrated along the boundaries between other gangue minerals in the breccia matrix (Figure 2a). Thin, acicular, or platy bastnäsite outgrow coarser aggregates of hematite, or form an interstitial network between quartz grains (Figure 2b,c). Exceptionally, as matrix bastnäsite becomes most abundant, it can appear as a fine-grained, aggregated cement for other minerals and/or clasts within the breccia (Figure 2d). In such cases, the clasts can contain a variety of other minerals including fluorite, hematite, U-minerals, and Cu-(Fe)-sulfides.

The fine-grained matrix bastnäsite is most pervasive in samples from the NW arm and central parts of the deposit consisting of breccias with granite or mafic clasts. In these samples, the bastnäsite matrix is concentrated within distinct, mm-scale, relatively porous zones that may represent pathways with enhanced permeability allowing greater fluid interaction (Supplementary Figure S1).

A second category of matrix bastnäsite occurs as stubby, coarser (tens to hundreds of μm in size) grains with euhedral tendency (Figure 3). Marked variations in grain size can co-exist whereby single, coarser grains feature minute inclusions and replacement by other gangue minerals (sericite, hematite), with which the smaller bastnäsite is intimately associated (Figure 3a). Such textural relationships suggest different generations of stubby bastnäsite formed during cycles of mineral growth/fluid percolation throughout the breccia matrix and around cavities (Figure 3b). Stubby bastnäsite is also

seen as more massive accumulations, forming a type of composite cement together with minor gangue minerals as part of the breccia matrix (Figure 3c,d). In such cases, the bastnäsite contains abundant, minute inclusions of a wide range of minerals, including sericite ± chlorite, hematite, as well as florencite, and occasional U-minerals (Figure 3c). Such inclusions can define grain-scale zonation, or growth stages within the stubby bastnäsite. These inclusions can result from replacement of pre-existing minerals during episodes of brecciation and milling such as seen in the case of magmatic zircon (Figure 3d). Stubby bastnäsite is best developed in samples from the NW arm (RX6709, RX6710, and RX6728). These samples are from breccias containing mafic clasts in which there is a marked lineation, again suggestive of enhanced fluid permeability (Supplementary Figure S1).

4.1.2. Irregular Bastnäsite Associated with Sulfides

Bastnäsite associated with Cu-Fe-sulfides (chalcopyrite and bornite) is highly irregular with respect to size and morphology (Figure 4). The sulfides can occur interstitial to bastnäsite aggregates, whereby scalloped boundaries are observed between the two minerals (Figure 4a,b). As in stubby bastnäsite, minute inclusions of other minerals can be locally abundant, including U-minerals, Cu-Fe-sulfides, and gangue minerals. In other cases, bastnäsite is present as sub-euhedral grains to patchy areas within sulfides (Figure 4c,d). In both cases the sulfide assemblage is from the intermediate zone of the orebody and consists of bornite with exsolutions of chalcopyrite, and adjacent chalcopyrite. Irregular bastnäsite is most pronounced in samples (samples RX6720-6722) from one drill core intersecting hematite-rich breccias from the center of the deposit towards the northern edge. These samples contain fluorite and quartz clasts, abundant coarse-grained hematite, and Cu-Fe-sulfides. Bastnäsite is concentrated within veinlets and pockets with sulfides.

4.1.3. Bastnäsite Replacing Breccia Clasts

Clast replacement bastnäsite (Figure 5) is observed in many samples, some of which also contain other forms of bastnäsite. When replacing clasts, bastnäsite displays textures that depend upon the mineralogy of the replaced clast. Outstanding examples show bastnäsite as bladed aggregates that pseudomorph the outline of the clast in hematite-rich breccias from the SE part of the deposit (sample RX6726; Figure 5a).

The clast is vuggy and includes sulfides (bornite + chalcocite). When occurring together with hematite, bastnäsite may adopt a feather-like intergrowth texture (Figure 5b). In breccias containing dyke clasts (sample 6723), bastnäsite occurs as an interstitial cement to euhedral grains of hematite (Figure 5c). Such clasts also include bornite + chalcocite intergrown with bastnäsite and minor quartz. Interestingly, wherever the bastnäsite is coarser and more euhedral, REE-rich lamellae or spots can be recognized within the grain core as brighter areas on the BSE images (Figure 5d). These are too small (<1 μm) to be analyzed by the present techniques but we can speculate they may represent a REE-oxyfluoride phase (haleniusite?) resulting from decarbonation. A variety of mineral assemblages can be found interstitial to the bastnäsite within the clasts and these include sericite, chlorite, quartz, Cu-(Fe)-sulfides, and hematite, as well as rarer rutile and synchysite.

4.2. Synchysite

Synchysite is a minor phase and is only observed in two samples, one from breccia containing dyke clasts (RX6714), and the second from hematite-rich breccia (RX6726). Both samples are located around the middle part of the deposit. Unlike bastnäsite, discrete grains of synchysite can be rarely observed as 10–50 μm-sized crystals within porous sericite or hematite. Importantly, the two BSG end-member species are present in both samples (Figure 6a,b). Synchysite occurs as patchy, interstitial filling between aggregates of bladed bastnäsite suggesting it is replaced by the latter (Figure 6a). However, in detail, the synchysite which is intergrown with chalcocite and sericite, locally replaces the adjacent bastnäsite lamellae (Figure 6b). It is interesting to note that minute inclusions of bornite and chalcocite are also present within the coarser bastnäsite.

High-magnification imaging at the direct contact between the two REE-fluorocarbonates shows even more complex textures (Figure 6c,d). Such textures include diffuse boundaries characterized by sets of sub-µm size, darker (Ca-bearing BSG species) lamellae within bastnäsite (Figure 6c). These boundaries are overgrown, in turn, by well-shaped bastnäsite grains. Another texture indicative of more complexity in terms of BSG speciation, are the µm-sized lamella edges on the margin of coarse bastnäsite showing compositional "polysynthetic twinning" between the dark and bright phases (Figure 6d). Such edges protrude into the immediately adjacent bornite. These sub-µm scale features are beyond the scope of the present study and will be addressed in future research.

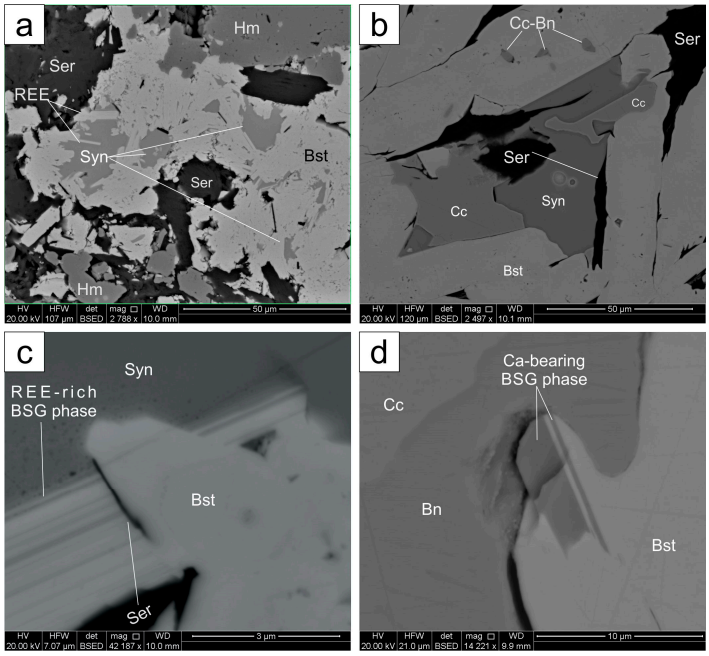

Figure 6. BSE images showing petrographic aspects of synchysite: (**a**) Synchysite (Syn) as patchy, interstitial filling between aggregates of bladed bastnäsite (Bst) (Sample RX6714). Hm-hematite, Ser-sericite; (**b**) Synchysite intergrown with chalcocite (Cc) and sericite locally replacing bastnäsite (sample RX6726). Bn-bornite; (**c**) Synchysite with intergrowths of a second REE-bearing phase (REE-rich BSG phase) along long axis. Sericite and bastnäsite crosscut both synchysite and REE intergrowths (sample RX6714); (**d**) Polysynthetic twinning between bright and dark phases. (Sample RX6726).

4.3. Other REE-Minerals

Although less abundant than bastnäsite, florencite is common throughout the sample suite. Florencite is usually anhedral and mostly occurs as fine-grained aggregates positioned between the coarser minerals. Florencite can occasionally be seen to overprint bastnäsite and synchysite but more often there are no clear relationships among the LREE-dominant minerals. Heavy REE-dominant minerals such as xenotime are relatively rare in these samples; xenotime is best preserved as overgrowths on zircon but can also be found together with coffinite, or included within bastnäsite. No monazite was observed in any of the samples investigated. Petrographic and compositional data for these minerals will be presented in a companion paper.

5. Compositional Data

The data presented here is strongly biased towards coarser REE-fluorocarbonates from samples that are particularly rich in REE-minerals. None of the small-scale intergrowths between bastnäsite and synchysite, or the REE-rich zones in bastnäsite have been analyzed as they are beyond the scope of the present study.

5.1. Bastnäsite-(Ce)

EPMA data for bastnäsite shows that all analyzed grains correspond to bastnäsite-(Ce) (Table 2). The complete analytical dataset for bastnäsite is given in Supplementary Table S5. In three single spot analyses, however, La slightly exceeds Ce, which is attributed to interference from the brighter REE-bearing phase exsolved in bastnäsite (Figure 5d). All analyzed grains are LREE-dominant with La/Ce ratio averaging ~0.61 (range 0.3–0.96). LREE abundances generally follow the order Ce > La > Nd > Pr > Sm > Eu. On average, (HREE + Y) makes up ~2.5% atoms per formula unit (a.p.f.u.) of total REE + Y.

Both Ca and Sr can be present at measurable concentrations in bastnäsite (up to 1.2 and 0.3 wt %, respectively). Time-resolved LA-ICP-MS depth profiles reveal that measured Fe, Si, and Al, which are other elements present at concentrations above EPMA mdl, relate to mineral inclusions and are hence not included in the calculated formulae. Bastnäsite formulae are calculated assuming full occupancy of one full position by REE, with CO_2 calculated on the basis of charge balance. An expanded representative formula for Olympic Dam bastnäsite-(Ce) is: $(Ca_{0.013}Sr_{0.001}La_{0.313}Ce_{0.488}Nd_{0.120}Pr_{0.043}Y_{0.012}Sm_{0.010}Gd_{0.005}Eu_{0.005}Dy_{0.002}Tb_{0.001}Er_{0.001})_{1.000}(F_{0.743}Cl_{0.002})_{0.745}(CO_3)$. Concentrations of F, as measured by EPMA, are consistently lower than the stoichiometric ideal and Cl contents are very low. One explanation may be diffusion away from the beam when using 20 s count times. Different F standards were tried to no avail, as was our attempt using different F standards against each other (i.e., using apatite as the F standard to calculate F for the EuF_3 standard), for which correct numbers were obtained. A second possibility is that full occupancy in the halogen site is met by (OH). This has, however, not been included in our calculation since the maximum limits of (OH) substitution in bastnäsite remain unknown [23–25].

5.2. Synchysite-(Ce)

EPMA data for the Ca-bearing REE-fluorocarbonates show they correspond to synchysite-(Ce) (Table 2, Supplementary Table S5). All analyzed grains are LREE-dominant, with mean La/Ce ratio of ~0.42 (range: 0.33–0.48), and LREE in order of abundances as Ce > La > Nd > Pr > Sm > Eu. (HREE + Y) makes up ~5% a.p.f.u. on average of the total REE + Y in synchysite. Measurable but minor Sr is present. Time-resolved LA-ICP-MS depth profiles show that the measured Fe relates to inclusions and this element is thus ignored in the calculated formulae. As with bastnäsite, concentrations of F are consistently lower than stoichiometric ideal (mean ~3.6 wt % F compared to ~6 wt % F in ideal end-member synchysite-(Ce)). Very minor concentrations of Cl, up to 0.03 wt %, were detected.

The structural formula for synchysite is calculated on the basis of and one divalent (Ca, Sr) and one trivalent (REE) cation with CO_2 calculated on the basis of charge balance. The mean empirical expanded formula for synchysite-(Ce) from Olympic Dam is thus: $(Ca_{0.998}Sr_{0.002})_{1.000}(La_{0.196}Ce_{0.471}Nd_{0.183}Pr_{0.055}Y_{0.029}Sm_{0.026}Gd_{0.017}Eu_{0.013}Dy_{0.006}Tb_{0.002})_{1.000}(F_{0.551}Cl_{0.001})_{0.552}(CO_3)_2$.

Of the two samples which contained abundant synchysite, RX6714 has generally higher La/Ce ratios and higher La, Ce, and HREE + Y values, while RX6726 had comparatively elevated contents of Nd, Sm, and Eu.

Table 2. Summary of EPMA compositional data for bastnäsite and synchysite. Average and standard deviations of major mineral groupings in weight percent (wt %) and atoms per formula unit (a.p.f.u.).

Mineral/Type	Bastnäsite										Synchysite	
	Matrix						Clast Replacement		Irregular			
	Stubby		Fine-Grained Cement		Disseminated							
	(n = 46)		(n = 93)		(n = 22)		(n = 66)		(n = 79)		(n = 20)	
	RX: 6709, 6710, 6728		RX: 6714, 6716, 6717, 6718, 6719, 6723, 6724, 6727		RX: 6711, 6712, 6715, 6723, 6725		RX: 6713, 6714, 6716, 6726		RX: 6720, 6721, 6722		RX: 6714, 6726	
(wt %)	Mean	St.dev.	Mean	St.dev.	Mean	St.dev.	Mean	St.dev.	Mean	St.dev.	Mean	St.dev.
Ca	0.04	0.02	0.35	0.21	0.29	0.33	0.23	0.14	0.32	0.19	12.30	0.58
Sr	0.03	0.03	0.07	0.04	0.08	0.06	0.05	0.02	0.05	0.02	0.05	0.01
La	17.03	1.65	21.97	3.63	15.38	2.27	19.93	2.38	22.49	1.86	9.88	1.23
Ce	33.77	2.00	33.13	2.80	33.49	1.63	34.34	2.06	32.00	1.22	23.76	1.20
Pr	3.61	0.18	2.74	0.44	3.56	0.49	3.14	0.36	2.67	0.19	2.67	0.15
Nd	10.91	1.18	7.29	1.97	11.06	2.11	8.91	1.67	7.39	0.74	8.91	0.79
Sm	0.95	0.31	0.57	0.33	1.16	0.38	0.84	0.34	0.55	0.15	1.18	0.18
Eu	0.44	0.14	0.28	0.12	0.48	0.10	0.43	0.16	0.25	0.08	0.56	0.10
Gd	0.36	0.21	0.33	0.21	0.60	0.29	0.43	0.24	0.30	0.11	0.77	0.13
Tb	0.07	0.02	0.07	0.02	0.09	0.03	0.08	0.03	0.07	0.02	0.09	0.02
Dy	0.18	0.09	0.15	0.09	0.27	0.14	0.19	0.08	0.14	0.05	0.34	0.08
Y	0.38	0.30	0.60	0.29	0.67	0.35	0.64	0.29	0.59	0.13	0.93	0.32
Ho	b.d.l.	b.d.l.	b.d.l.	b.d.l.	b.d.l.	b.d.l.	b.d.l.	b.d.l.	0.14	0.00	0.13	0.00
Er	0.084	0.02	0.08	0.02	0.09	0.03	0.08	0.03	0.08	0.02	0.09	0.02
Tm	b.d.l.	b.d.l.	0.07	0.01	b.d.l.	b.d.l.	0.05	0.00	0.064	0.01	b.d.l.	b.d.l.
Yb	0.07	0.00	0.07	0.02	b.d.l.	b.d.l.	0.49	0.43	0.08	0.01	b.d.l.	b.d.l.
F	7.35	0.14	7.19	0.30	7.24	0.34	7.25	0.23	7.15	0.17	3.62	0.46
Cl	0.02	0.01	0.04	0.02	0.03	0.02	0.03	0.01	0.03	0.02	0.02	0.01
Na	b.d.l.	b.d.l.	0.10	0.11	0.11	0.05	b.d.l.	b.d.l.	0.03	0.00	b.d.l.	b.d.l.
Al	0.18	0.23	0.20	0.26	0.10	0.09	0.34	0.62	0.67	1.80	0.30	0.36
K	0.01	0.00	0.05	0.09	0.06	0.04	0.03	0.05	0.06	0.24	0.07	0.08
Fe^{3+}	0.25	0.21	0.33	0.41	0.57	0.37	0.30	0.32	0.47	0.74	0.11	0.06
S	0.04	0.02	0.03	0.02	0.05	0.03	0.07	0.21	0.02	0.02	0.01	0.00
U	b.d.l.	b.d.l.	0.33	1.11	0.06	0.03	0.06	0.03	0.17	0.09	0.03	0.00
Th	0.08	0.07	0.11	0.09	0.43	0.32	0.16	0.12	0.07	0.04	0.05	0.00
Pb	b.d.l.	b.d.l.	0.03	0.01	0.04	0.01	b.d.l.	b.d.l.	0.05	0.02	b.d.l.	b.d.l.
Measured Total	75.30	2.12	75.30	3.28	75.41	3.66	76.98	2.64	74.66	2.76	65.32	2.04
∑REE + Y	67.62	2.15	67.18	3.75	66.79	3.61	69.06	2.82	66.48	2.50	48.20	1.95
La/Ce	0.51	0.06	0.67	0.15	0.46	0.06	0.58	0.09	0.70	0.05	0.42	0.05
CO_2 wt %	21.20	0.68	21.16	1.17	20.96	1.13	21.71	0.88	20.94	0.78	28.98	0.99
Calc. Total	96.24	2.81	95.98	4.78	95.38	4.84	98.32	3.76	94.96	3.30	94.09	2.92
(a.p.f.u.)												
Ca	0.002	0.001	0.018	0.010	0.014	0.016	0.011	0.007	0.016	0.009	0.998	0.001
Sr	0.001	0.001	0.002	0.001	0.002	0.001	0.001	0.001	0.001	0.000	0.002	0.001
Total 2+	0.002	0.001	0.020	0.011	0.016	0.017	0.012	0.008	0.017	0.010	1.000	0.000
La	0.254	0.023	0.329	0.050	0.233	0.034	0.291	0.032	0.340	0.022	0.202	0.021
Ce	0.500	0.026	0.492	0.031	0.502	0.018	0.497	0.024	0.480	0.006	0.483	0.011
Pr	0.053	0.003	0.040	0.006	0.053	0.006	0.045	0.005	0.040	0.003	0.054	0.003
Nd	0.157	0.016	0.105	0.027	0.161	0.027	0.125	0.022	0.108	0.011	0.176	0.017
Sm	0.013	0.004	0.008	0.004	0.016	0.005	0.011	0.004	0.008	0.002	0.022	0.004
Eu	0.006	0.002	0.004	0.002	0.007	0.001	0.006	0.002	0.003	0.001	0.011	0.002
Gd	0.005	0.003	0.004	0.003	0.008	0.004	0.005	0.003	0.004	0.001	0.014	0.002
Tb	0.001	0.000	0.001	0.000	0.001	0.000	0.001	0.000	0.001	0.000	0.002	0.000
Dy	0.002	0.001	0.002	0.001	0.003	0.002	0.002	0.001	0.002	0.001	0.006	0.001
Y	0.009	0.007	0.014	0.007	0.016	0.008	0.014	0.007	0.014	0.003	0.030	0.010
Ho	b.d.l.	b.d.l.	b.d.l.	b.d.l.	b.d.l.	b.d.l.	b.d.l.	b.d.l.	0.002	0.000	0.000	0.000
Er	0.001	0.000	0.001	0.000	0.001	0.000	0.001	0.000	0.001	0.000	0.001	0.001
Tm	b.d.l.	b.d.l.	0.001	0.000	b.d.l.	b.d.l.	0.001	0.000	0.001	0.000	0.000	0.000
Yb	0.001	0.000	0.001	0.000	b.d.l.	b.d.l.	0.006	0.005	0.001	0.000	0.000	0.000
Total 3+	0.998	0.001	0.980	0.011	0.984	0.017	0.988	0.008	0.983	0.010	1.000	0.000
F	0.802	0.030	0.774	0.055	0.790	0.060	0.765	0.031	0.777	0.031	0.545	0.079
Cl	0.001	0.000	0.002	0.001	0.002	0.001	0.002	0.001	0.002	0.001	0.001	0.001
F+Cl	0.803	0.030	0.776	0.055	0.791	0.059	0.767	0.031	0.779	0.031	0.546	0.079

* b.d.l.—below detection limit. Si, As, P, Zr were all b.d.l.

5.3. Trace Element Concentrations

Concentrations of trace elements in bastnäsite and synchysite are minor and display significant variance both within and between samples. Nevertheless, distinctions between the mineral classes can be recognized (Table 3). The full LA-ICP-MS dataset is given as Supplementary Table S6.

Stubby matrix bastnäsite, occurring together with barite, contains less Ca as well as elevated Sr (mean 531 ppm), thus a greater Sr/Ca ratio on average compared to the other bastnäsites (Table 3, Figure 7a). Stubby matrix bastnäsite is also distinguished by elevated Th (mean 213 ppm) compared to U (mean 28 ppm), which is the lowest amount of U of all the bastnäsite. Fine-grained matrix cement bastnäsite has significantly more Th to U (533 and 388 ppm, respectively), which is also the highest Th of all bastnäsite types. The clast replacement bastnäsite has almost equal mean Th and U (272 and 266 ppm, respectively) while irregular bastnäsite has vastly more U than Th (mean 1840 and 78 ppm, respectively) and both the lowest Th and highest U means of all bastnäsite. Compared to the bastnäsite values, synchysite is low in both U and Th, but with more than three times as much U than Th (mean 62 and 20 ppm, respectively) (Figure 7b). Time-resolved downhole laser profiles show that U and Th can occur both within sub-microscopic mineral inclusions and within the lattice of the bastnäsite (Supplementary Figure S2). The profiles suggest that in the coarser-grained bastnäsite, stubby matrix and clast replacement, much of the U and Th is inclusion-hosted, while lattice-hosted U and Th dominates in fine-grained matrix cement or irregular bastnäsite. The sericitized dyke, included in the fine-grained cement bastnäsite group, has bastnäsite that most consistently includes measurable proportions of ^{204}Pb as well as ^{206}Pb, ^{207}Pb, and ^{208}Pb. On average, sodium is higher in the fine-grained cement bastnäsite; of the bastnäsites, P and Zr are higher in matrix stubby and fine-grained bastnäsite but Zr is highest in synchysite. All other trace elements analyzed were extremely low (e.g., Nb), consistently < mdl (e.g., Sc), or entirely present in the form of mineral inclusions (e.g., Fe, Al, and Si).

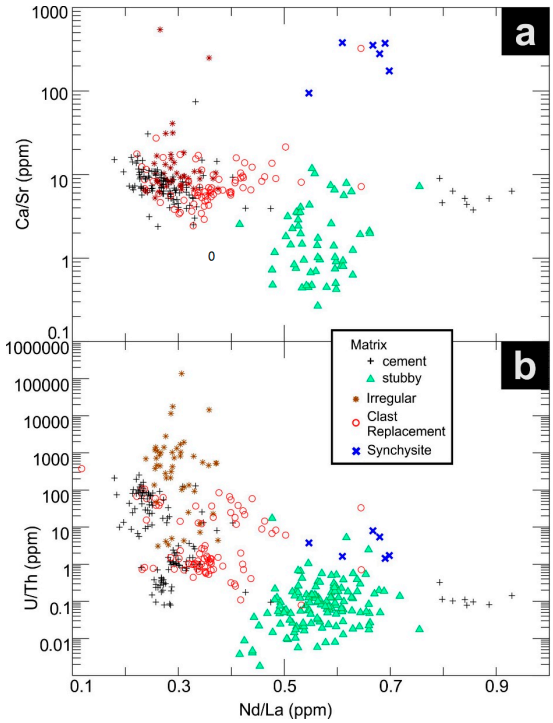

Figure 7. Trace element ratios in bastnäsite and synchysite: (**a**) Ca/Sr vs. Nd/La. Note most stubby matrix bastnäsite is richer in Sr compared to Ca; (**b**) U/Th vs. Nd/La. Note that relative proportions of U to Th separate the textural groupings with the irregular, sulfide-associated group containing more U compared to Th. The stubby matrix group, and to a lesser extent, the clast replacement sub-type, contains more Th than U.

Table 3. Summary of LA-ICP-MS trace element data for bastnäsite and synchysite. Mean, minimum (min), and maximum (max) values for major mineral groupings (in ppm).

Mineral/Type	Bastnäsite														
	Matrix						Clast Replacement			Irregular			Synchysite		
	Stubby			Fine-Grained Cement											
	(n = 137)			(n = 123)			(n = 84)			(n = 49)			(n = 6)		
	RX: 6709, 6710, 6728			RX: 6714, 6716, 6717, 6718, 6719, 6723, 6724, 6727			RX: 6713, 6714, 6716, 6726			RX: 6720, 6721, 6722			RX: 6714		
	Mean	Min.	Max.	Mean	Min.	Max.	Mean	min.	Max.	Mean	Min.	Max.	Mean	Min.	Max.
La	180,000	139,700	237,000	233,000	102,800	320,000	235,000	159,000	395,000	241,000	213,100	271,000	117,900	114,200	123,000
Pr	35,300	29,380	40,600	26,900	11,800	37,960	30,700	21,800	58,100	26,600	24,000	29,400	25,000	21,700	26,140
Nd	101,400	78,000	124,000	67,600	29,140	129,000	81,200	43,200	163,000	71,200	64,400	86,900	76,500	62,400	83,500
Sm	9170	5520	13,200	5760	2860	16,600	7500	1860	16,800	6230	4670	8520	9140	6550	10,500
Eu	2790	1460	4820	1710	435	4820	2510	347	7200	1700	870	2690	3160	2110	3680
Gd	3290	1470	5720	2870	1190	8420	3480	627	9820	3220	2270	4700	5660	3680	6550
Tb	289	93.2	561	302	95.4	819	343	41.4	830	320	218	455	684	376	835
Dy	1180	278	2340	1430	335	3510	1480	153	3290	1440	1020	1890	3230	1630	3890
Y	2990	664	6450	5170	1030	10,600	4230	378	11,600	5320	3860	7370	9050	3430	11,500
Ho	161	29.0	324	216	39.1	456	210	19.2	460	225	156	309	420	189	545
Er	313	44.4	682	466	55.9	920	430	36.7	935	512	309	757	695	297	1003
Tm	28.2	3.0	66.0	44.9	3.8	106	42.0	2.7	108	53.6	25.6	91.9	49.9	21.5	74.0
Yb	129	13.0	322	219	12.6	620	211	11.4	617	284	105	623	178	75.0	290
Lu	13.3	1.0	34.9	23.5	1.2	72.3	21.7	1.1	60.8	33.6	12.5	90.0	13.3	5.9	26.2
Ca	897	158	3100	3980	820	9950	2290	790	6100	3920	1440	9800	111,000	20,200	155,000
Sr	531	27.1	6500	591	26.9	2940	294	24.1	752	377	217	872	427	214	890
Th	213	0.14	4960	533	0.23	3760	272	0.08	5290	78.3	0.88	619	20.2	8.3	29.5
U	28.1	0.07	1510	388	7.4	7200	266	1.5	1040	1840	781	10,100	62.3	29.0	114
Pb	36.2	1.8	606	352	5.2	1370	196	1.0	2840	751	422	2150	23.7	3.0	69.5
Ba	108	0.67	7000	266	0.53	2320	82.7	0.5	1560	47.4	5.0	205	182	22.9	690
Mn	10.8	0.50	126	21.4	3.9	142	19.5	2.7	450	19.2	3.5	147	48.6	18.6	78.5
Na	229	8.5	2910	710	71.0	3250	449	69.0	3740	260	83	1100	59.0	59.0	59.0
Nb	17.0	0.1	250	6.1	0.09	150	19.0	0.07	560	2.4	0.22	10.2	3.6	0.66	7.4
P	1730	52.0	31,400	1450	69.0	9700	260	260	260	275	75.0	1100	b.d.l.	b.d.l.	b.d.l.
Zr	20.7	0.09	1220	5.0	0.11	110	5.1	0.10	155	0.42	0.10	0.84	258	4.5	690

b.d.l.—below detection limit. Si, As, P, Zr were all b.d.l.

5.4. Compositional Trends and Chondrite-Normalized Fractionation Patterns

Subtle compositional variation is present between the different textural forms of bastnäsite. There is a progressive change in the dominant REE (La, Ce, and Nd) from types containing more La towards those relatively enriched in Ce and Nd (Figure 8a). Fine-grained matrix cement (Figure 2) and irregular bastnäsite (Figure 4) are the richest in La, with Ce and Nd increasing through clast replacement bastnäsite (Figure 5), disseminated matrix and stubby bastnäsite (Figure 3), to synchysite (Figure 6), which contains the most Nd. Synchysite consistently contains more Nd and less La compared to most bastnäsite (Figure 8a). Fine-grained disseminated and stubby matrix bastnäsite show considerable overlap in La-Ce-Nd composition, as do irregular and fine-grained cementing matrix bastnäsite, with clast replacement bastnäsite positioned between those two groups. While maintaining similar La/Ce values, the irregular and fine-grained cement matrix bastnäsite are separated by their slight differences in Nd values, with irregular bastnäsite being slightly more elevated in that element (Figure 8b). Stubby matrix bastnäsite shows a deviation from other fluorocarbonates on Figure 8c, plotting below the curve, with lower La relative to other LREE if compared to the other bastnäsite types.

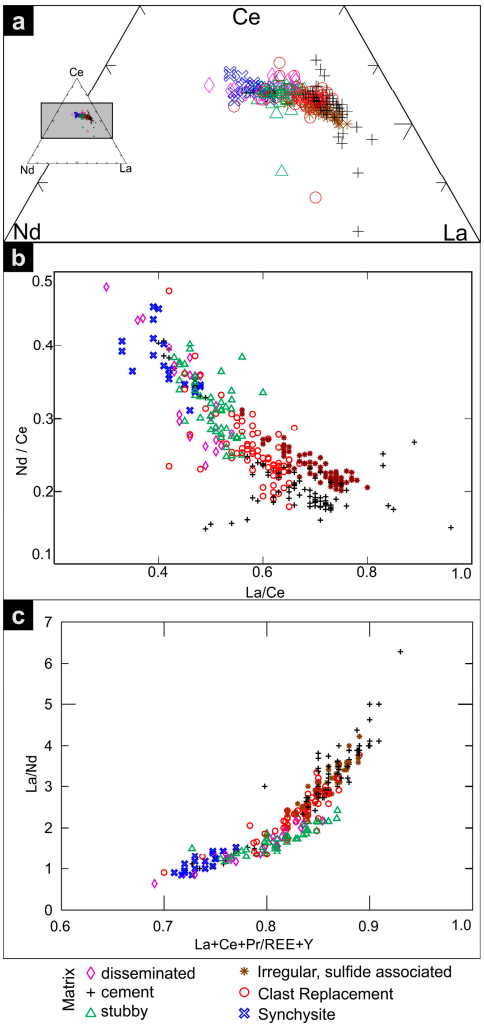

Figure 8. REE compositions of bastnäsite and synchysite (EMPA data, a.p.f.u.): (**a**) Ternary Nd-Ce-La plot showing progression of bastnäsite sub-groups from Ce- and Nd- to La-enriched; (**b**) La/Ce vs. Nd/Ce showing clustering of bastnäsite textural groups and separation of irregular and fine-grained cement bastnäsite; (**c**) Relative LREE ratios (after [35]) showing a continuous curve through synchysite, clast replacement, irregular, and fine-grained matrix bastnäsite, and stubby bastnäsite plotting astray from the curve.

When comparing the full spectrum of REE (using concentrations measured by LA-ICP-MS for those at lowest concentrations), the fine-grained matrix cement and irregular bastnäsite show elevated (HREE + Y) relative to MREE, and also greater La enrichment compared to clast replacement bastnäsite and stubby matrix bastnäsite (Figure 9a). Synchysite plots closer to stubby matrix bastnäsite albeit with slightly elevated (HREE + Y). Within the stubby matrix bastnäsite there are some compositional differences between bastnäsite formed in cavities and those within the matrix; cavity bastnäsite shows relatively elevated La and Ce and depletion in the other REE.

Chondrite-normalized fractionation trends show subtle variations in the different bastnäsite groups and synchysite (Figure 9b). The more LREE-enriched stubby bastnäsite can be distinguished from the slightly more HREE-enriched fine-grained matrix cement and irregular bastnäsite. Synchysite is shown to be enriched in only certain HREE (Dy, Y, and Ho) and is depleted in LREE and Tm, Yb, and Lu relative to bastnäsite. Synchysite and stubby bastnäsite show similar chondrite-normalized patterns although synchysite is richer in MREE and stubby bastnäsite is richer in LREE (Figure 9b). Chondrite-normalized fractionation patterns of the fine-grained matrix cement and irregular bastnäsite are similar, with slight separation among the heaviest HREE. Clast replacement bastnäsite shows similarity to the stubby bastnäsite group in the LREE segment but becomes more HREE-enriched. Stubby bastnäsite and synchysite have similar Y/Ho ratios, and more pronounced negative Y-anomaly than the irregular and fine-grained matrix cement, which shows flatter patterns and smaller Y-anomalies.

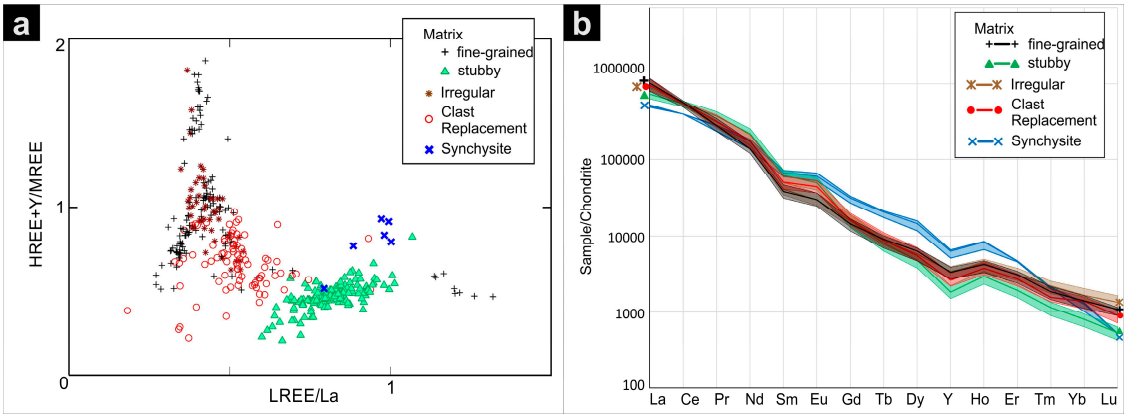

Figure 9. Compositional variation (LA-ICP-MS data) for REE in bastnäsite and synchysite; (**a**) (HREE + Y)/MREE vs. LREE/La, where HREE = (Tm + Yb + Lu + Y), MREE = (Gd + Tb + Dy + Ho + Er), and LREE = (Pr + Nd + Sm). LREE/La separates out those grains relatively enriched in La (irregular, fine-grained cement and clast replacement bastnäsite) from those with a more diverse LREE signature (stubby matrix bastnäsite and synchysite). The plot also exposes the relative enrichment in (HREE + Y) in irregular and fine-grained cement bastnäsite (those with highest HREY/MREY are fine-grained cements from sample RX6724) and relative MREE enrichment in stubby matrix bastnäsite and synchysite. Fine-grained cement bastnäsite with high (Pr + Nd + Sm) plots at the extreme right (sample RX6723); (**b**) Chondrite-normalized REY fractionation trends for the different groups of REE-fluorocarbonates (LA-ICP-MS data). Chondrite values after [36]. See also text for additional explanation.

6. Discussion

6.1. Data Trends

REE-fluorocarbonates from Olympic Dam are Ce-dominant but there is nevertheless a subtle yet measurable variation in the relative abundances of the different REE + Y within these minerals from different samples. Bastnäsite and synchysite compositions show consistent compositional differences and clustering on the plots which can be correlated with textures. Synchysite, disseminated matrix

bastnäsite, and stubby bastnäsite cluster together forming one field, while irregular, sulfide-associated and fine-grained matrix cement bastnäsite cluster within a second field. Compositions of clast replacement bastnäsite typically fall between the two groups, or tend to spread across both. The clustering of the mineral groups is consistent on all plots (Figures 7–9), and although this may yet be better exposed by a more extensive sample set, we believe these patterns carry genetic significance. Stubby bastnäsite and synchysite are clearly separated from the other bastnäsite categories. Texturally, these two groups are probably earlier—possibly linked to hydrothermal alteration of granites, with Ca for synchysite being sourced from the replacement of plagioclase feldspar. The other categories of bastnäsite are thus later and are associated with subsequent stages of IOCG deposit evolution, including the late deposition of chalcocite-bornite assemblages at shallow levels.

Smith et al. [35] report variation in REE-fluorocarbonate composition from Bayan Obo. Decrease in La/Nd is inferred to reflect changes in fluid composition from CO_2-rich hydrothermal fluids to aqueous solutions, and a decrease in temperature. Compositions are controlled by changes in REE speciation in the hydrothermal fluid, and the relative solubilities of those species and precipitated REE minerals. Smith et al. [35] model La/Nd fractionation and believe that it should be recognized in other REE-rich hydrothermal systems. We believe that our work goes some way to recognizing similar trends at Olympic Dam. The unequivocal positioning of distinct REE-fluorocarbonate compositions within the temporal-spatial development of the deposit is, however, hampered by the superimposed cycles of replacement and recrystallization recognized in many component minerals at Olympic Dam.

Apart from Ca, Sr, Th, and U, the REE-fluorocarbonates generally contain negligible trace elements at measurable concentrations. Elements that might have been expected within these REE minerals, notably Sc, As, and Nb, would appear to have partitioned into other co-existing minerals. Thorium and U is always present, although often at concentrations of only a few ppm.

Synchysite is restricted in its occurrence at Olympic Dam compared to the ubiquitous bastnäsite. When present, the relationship between the two minerals is often ambiguous, although synchysite may appear crosscut by larger grains of bastnäsite. The temporal relationship between the two minerals requires further work to be properly assessed.

Pseudomorphic replacement of feldspars by micron- to lattice-scale intergrowths among BSG species in the compositional range between parisite and bastnäsite is documented from a distal satellite (mineralized red-stained granite interval) at Olympic Dam [13,33]. These assemblages, which are associated with sericite, molybdenite, and hematite, prove the point that during the early stages of granite alteration, in which plagioclase feldspars are replaced but K-feldspars are still present, the REE-fluorocarbonates are Ca-bearing.

Synchysite from the OD orebody is distinctly poorer in La and richer in Nd and Ce than bastnäsite where they co-exist spatially, mostly as clast replacement (Figures 5a and 6b,d). Ca^{2+} is required for precipitation of synchysite, and needs to be unavailable to allow bastnäsite to form. Variation in aCa^{2+}, together with aCO_3 and aF, thus defines the stability fields for minerals across the BSG group [22]. Bastnäsite occurs in samples with abundant fluorite which could explain why no Ca-bearing REE-fluorocarbonates are present if the two minerals are precipitated simultaneously. Such an assumption implies high F activity e.g., $\log aF > -3$ at 300 °C; in a fluorocarbonate–CO_2–fluid buffered system at a pH of ~4.5 to 5.2 concordant with sericite stability [22]. The limited occurrence of synchysite in this sample set may suggest that formation is constrained by the local assemblage and limited availability of Ca, such as during the early albitization event leading to replacement of plagioclase feldspar [12].

6.2. Comparison with Published Compositional Data

The volume of published compositional data for bastnäsite and synchysite is rather limited but nonetheless instructive, as it demonstrates both the variability in natural REE-fluorocarbonates and the dependence of composition on the formational environment and conditions. The La/Nd ratio in REE-fluorocarbonates is used to identify and define variable hydrothermal systems and REE

fractionation within, or between deposits. Fleischer [37] reports compositional variability among REE-fluorocarbonates from different rocks using La/Nd as a "useful indicator of paragenetic type of occurrence". Others (e.g., [35,38]) have shown that changes in this ratio represent a useful indicator of evolving conditions, and can also be used to interpret fluid compositions and temperature. Figure 10 compares the La/Nd and La/Ce ratios of Olympic Dam synchysite and bastnäsite from this study with published datasets for the two minerals.

Most published work on synchysite has proposed that REE are leached from the host rock and precipitated as independent REE-minerals. Carbonatites are typified by greater enrichment in La compared to other deposit types. The "hydrothermal" group displays the least enrichment in La. "Hydrothermal" synchysite, in which REE is sourced from fluids associated with igneous host rocks (syenite, granite) has average ratios La/Nd of 1.157 and La/Ce ratios of 0.470 [39–41]. In contrast, carbonatite-hosted synchysite has average La/Nd and La/Ce ratios of 2.471 and 0.617, respectively [42,43]. Pegmatite-hosted synchysite [44] has average La/Nd and La/Ce ratios of 1.692 of 0.524; synchysite precipitated in basalts has average ratios of La/Nd = 1.459 and La/Ce = 0.543 [45]. Lastly, synchysite from hydrothermal fluorite veins, where REE are thought not to have been sourced not from the host rocks but rather from the basement, has average La/Nd as 1.238 and La/Ce 0.525 [46]. Average La/Nd and La/Ce ratios in Olympic Dam synchysite are 1.147 and 0.419, respectively, within the field of published data for occurrences associated with felsic intrusive rocks (Figure 10).

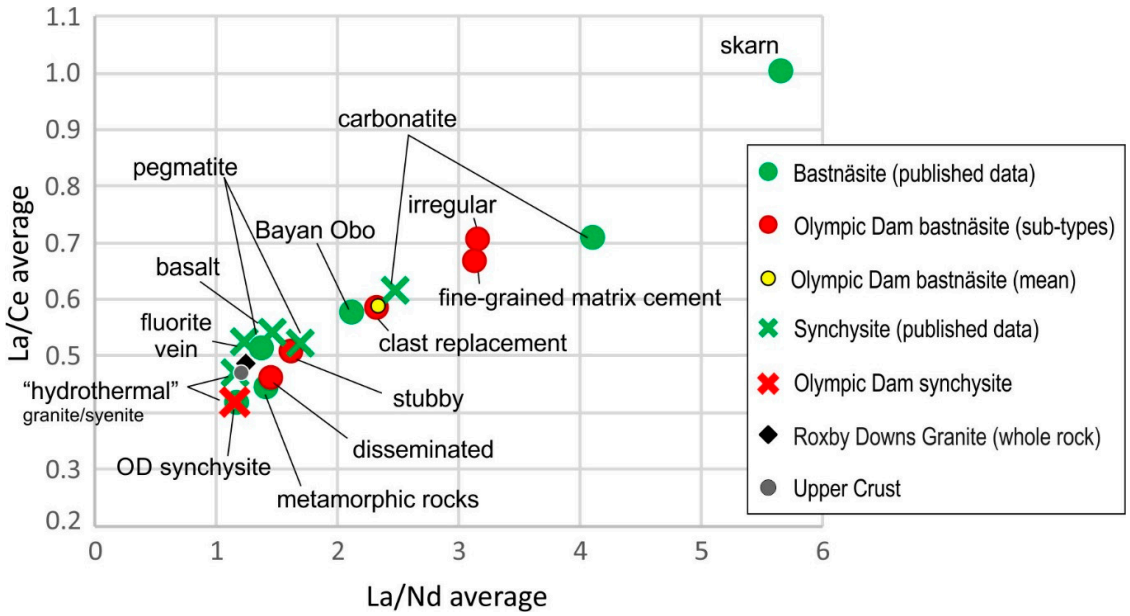

Figure 10. Plot showing mean La/Ce and La/Nd ratios in bastnäsite and synchysite from published data [35,38–48] compared to measured ratios from Olympic Dam (this study). See text for details.

Published compositional data for bastnäsite tend to be more varied than for synchysite, but overall, data for carbonatite-hosted bastnäsite [42], skarn bastnäsite [38], and from Bayan Obo [35] have higher La/Nd (4.103, 5.653, and 2.117, respectively) than bastnäsite associated with felsic intrusions: pegmatites [47]; alkaline igneous rocks [40]; or metamorphic rocks [48], which have lower La/Nd (1.372, 1.162, and 1.424, respectively). The distinction in terms of La/Ce ratios is less marked but ratios for intrusion-associated bastnäsite are nevertheless lower than for carbonatite- and skarn-hosted types. Figure 10 shows that different textural types of Olympic Dam bastnäsite plot apart on the diagram, within the fields of both carbonatite and hydrothermal bastnäsite. Despite the clear discrimination suggested by using average values on the plot, variability in bastnäsite compositions across a broad range of values appears characteristic of many other occurrences and may be attributed to changes in fluid composition, temperature, or pH.

Figure 10 shows a continuum of these ratios from more La-rich to La-poor/Nd- and Ce-enriched in different deposit types. Generally, carbonatite-hosted REE-fluorocarbonates display La-enrichment, even if published data suggests that skarn bastnäsite is even more elevated in La. Synchysite is concentrated towards the lower La/Nd and La/Ce corner, with Olympic Dam synchysite having the lowest values of both ratios. Whole-rock La/Nd and La/Ce ratios of the Roxby Downs Granite (RDG), which hosts the ODBC and thus the orebody, are also plotted on Figure 10. The RDG has ratios close to that of the average upper crust RDG La/Nd = 1.248, La/Ce = 0.487, avg. upper crust La/Nd = 1.2, La/Ce = 0.47 [38] and plots within that part of the diagram with the greatest concentration of data points, also close to the average for Olympic Dam synchysite. The average composition of Olympic Dam bastnäsite is also close to the average for the giant REE deposit of Bayan Obo [35]. This observation is particularly interesting in light of the hypothesis [49] that there should be a communality of fluid compositions associated with IOCG deposits *sensu stricto* and carbonatite-hosted ore systems such as Bayan Obo and Phalaborwa, South Africa.

The mean Y/Ho ratio of Olympic Dam REE-fluorocarbonates (20.8, std. dev. 3.4) is lower than the CHArge-and-RAdius-Controlled (CHARAC; [50]) trace element behavior field (24 < Y/Ho < 34) and "bulk earth" (Y/Ho = 28) [50,51]. Olympic Dam REE-fluorocarbonates thus fall within the field of hydrothermal carbonates [50]; magmatic and marine sedimentary carbonates Y/Ho values are within and above the CHARAC field, respectfully [50,51].

6.3. Formation Conditions

The deviation of bastnäsite from the whole-rock ratio of host RDG demonstrates a fractionation across the deposit which could have several causes: an evolution of bastnäsite crystallization in space and/or time, control by local conditions, or partitioning with co-existing phases. Despite the deposit showing an overall enrichment in LREE relative to HREE, REE fractionation is reported for other minerals from Olympic Dam. Distinct LREE depletion and relative MREE-enrichment are documented from hydrothermal apatite associated with hematite-sericite alteration and high-grade ore [11]. This was taken to support LREE transport as soluble chloride complexes, with which LREE are most compatible and remain in solution at high temperatures [43,52,53]. McPhie [54] extrapolate data for melt inclusions containing fluorite to claim that hydrothermal fluids at Olympic Dam were strongly acidic and very rich in F. Although this is yet to be unequivocally proven for the hydrothermal stages at OD, the presence of abundant fluorite throughout parts of the ODBC, including within the samples studied here, allows for an interpretation in which F-rich hydrothermal fluids were present at least during some stages of breccia formation and ore deposition. Under such conditions, it likely that the REE were mobilized and bastnäsite-Ce deposited by the reaction: $REECl_2^+ + HF + HCO_3^- = REECO_3F + 2H^+ + Cl^-$ [53]. REE-chloride complexes dominate under acidic conditions [55] and precipitation of REE minerals could be initiated via an increase in pH or $(CO_2)^-$ activity or a decrease in Cl-activity, with fluoride acting as a binding ligand to promote mineralization [53].

The dominance of REE-fluorocarbonates over other REE-minerals also suggests high aCO_2. While Olympic Dam contains abundant carbonates [7,32], the deposit lacks (carbonatite) carbonate, as at Bayan Obo [35], or limestone in the Bastnäs Fe-Cu-REE skarn deposit [38] to supply HCO_3. We can therefore presume that CO_2 was supplied by the hydrothermal fluids.

Changes in fluid redox or pH conditions should be exposed through marked Ce- or Eu-anomalies on the chondrite-normalized fractionation patterns. Such anomalies are, however, not observed for REE-fluorocarbonates from Olympic Dam, suggesting that these conditions are unlikely to have driven REE-fluorocarbonate deposition. This is indirectly corroborated by the interpretation that albitization is controlled by pH and not by a change in redox conditions [12]. Similarly, the influence of high pH, rather than redox, on CO_2-buffered fluids is proposed to have caused fractionation of MREE-rich apatite in high-grade bornite ores [11].

The source of REE concentrated within the Olympic Dam deposit is granite-related, either directly from hydrothermal fluids, or via hydrothermal alteration and breakdown of granite-forming minerals,

notably feldspars [12]. Bastnäsite is not a secondary mineral formed via alteration or replacement of a pre-existing REE mineral, but rather a primary LREE phase. Such a scenario does not discount the possibility of a precursor LREE mineral phase, such as monazite, that has since been altered or dissolved, with LREE "recycled" into synchysite (e.g., [56]) or bastnäsite. There is, however, no direct evidence of synchysite or bastnäsite replacing monazite or any other LREE-bearing mineral, apart from bastnäsite replacing synchysite. Broadly similar hydrothermal fluids and physicochemical conditions coincided with the stability field of bastnäsite, leading to its dominance over other REE-minerals across the deposit. The high-grade REE zones studied here may be attributed to enhanced permeability/porosity, and potentially to localized conditions promoting REE deposition.

6.4. Implications

The reproducible compositional differences among textural groups of REE-fluorocarbonates from Olympic Dam carry several implications for fluid evolution. Some texturally and compositionally distinct bastnäsite groupings are restricted to narrow intersections, only a few cm across, in just one or two drill holes (stubby and irregular, sulfide-associated), indicating a degree of spatial control. Other compositionally distinct textural types (matrix fine-grained disseminated and cement and clast replacement) are more widespread across the deposit. Because of the limited and highly targeted sample set, it is difficult to say if these are true clusters or only points on a continuous spectrum. Bastnäsite textures are highly dependent on co-existing mineral assemblages; fine-grained bladed bastnäsite develops within fine-grained sericite-dominant matrices and coarser crystals also occur, suggesting that relative REE and trace element concentrations may be dependent on co-existing minerals.

The absence of monazite in the studied samples is conspicuous and will be examined, together with the petrography of florencite, xenotime and other phosphates, which commonly replace the REE-fluorocarbonates, in a subsequent companion publication.

7. Conclusions

1. Bastnäsite-(Ce) is the most abundant REE-fluorocarbonate across the Olympic Dam deposit; synchysite-(Ce) is subordinate. Representative formulae for Olympic Dam bastnäsite-(Ce) and synchysite-(Ce) are: $((Ca,Sr_{0.01})La_{0.31}Ce_{0.49}Nd_{0.12}RE^*_{0.08})_{1.00}(F,Cl)_{0.75}(CO_3)$ and $(Ca,Sr)_{1.00}(La_{0.20}Ce_{0.47}Nd_{0.18}RE^*_{0.15})_{1.00}(F,Cl)_{0.55}(CO_3)_2$, respectively [RE* = REE other than La, Ce, and Nd]. Both show significant deficiencies in the halogen site, which may possibly be due to F migration under the beam, or met by hydroxl ions.
2. Bastnäsite occurs in a range of different textural forms, defined here as matrix, including fine-grained disseminated matrix, fine-grained cement matrix, and stubby matrix, as well as irregular bastnäsite associated with sulfides, and clast replacement bastnäsite. Textures and occurrences of bastnäsite at Olympic Dam are largely driven by the specific location and prevailing mineral assemblage, with morphology and grain size often controlled by the associated minerals (hematite, sulfides). High REE-grade zones formed due to enhanced permeability/porosity and localized conditions that promoted REE deposition.
3. Compositionally, REE-fluorocarbonates define a spectrum from relatively La-enriched to (Ce + Nd)-enriched minerals, although Ce is the dominant element in all grains analyzed. The fractionation of REE in bastnäsite and synchysite may reflect two distinct episodes of precipitation during the IOCG-forming event. The earlier, represented by stubby bastnäsite and synchysite may be associated with hydrothermal alteration of granite and Ca release from plagioclase, whereas the latter (bastnäsite only) is contemporaneous with the onset of sulfide deposition.

Supplementary Materials: The following are available online at www.mdpi.com/2075-163X/7/10/202/s1, Supplementary Material 1: Analytical Methods, Electron Probe Microanalysis, Supplementary Material 2: Analytical Methods, Laser Ablation Inductively Coupled Mass Spectrometry; Table S1: Sample XRD data,

Table S2: Full details of analytical set-up for EPMA analysis, Table S3: Full EPMA standard list, Table S4: Full details of analytical set-up for LA-ICP-MS analysis, Table S5: Complete EPMA dataset for REE-fluorocarbonates, Table S6: Full LA-ICP-MS dataset for REE-fluorocarbonates; Figure S1: Detailed images of the sample set, Figure S2: Examples of LA-ICP-MS downhole laser profiles.

Acknowledgments: This research is a contribution to the ARC Research Hub for Australian Copper–Uranium, co-supported by BHP Olympic Dam and the South Australian Mining and Petroleum Services Centre of Excellence. We thank two anonymous Minerals reviewers for their helpful comments which helped us improve this manuscript.

Author Contributions: Danielle S. Schmandt performed all analytical work and data processing under the guidance of Benjamin P. Wade and Sarah Gilbert. Nigel J. Cook and Kathy Ehrig devised the project; Kathy Ehrig and Vadim S. Kamenetsky contributed samples and deposit information; Danielle S. Schmandt, Nigel J. Cook and Cristiana L. Ciobanu wrote the paper, assisted by all other authors. This research forms part of the Ph.D. project of Danielle S. Schmandt.

Conflicts of Interest: The authors declare no conflict of interest. The project sponsors approve publication of the manuscript.

References

1. BHP Annual Reporting Suite 2016. Available online: http://www.bhp.com/investor-centre/annual-reporting-2016 (accessed on 27 September 2017).
2. Williams, P.J.; Barton, M.D.; Johnson, D.A.; Fontbote, L.; de Haller, A.; Mark, G.; Oliver, N.H.S.; Marschik, R. Iron Oxide Copper-Gold Deposits: Geology, Space-Time Distribution, and Possible Modes of Origin. *Econ. Geol.* **2005**, *Anniversary*, 371–405.
3. Groves, D.I.; Bierlein, F.P.; Meinert, L.D.; Hitzman, M.W. Iron Oxide Copper-Gold (IOCG) Deposits through Earth History: Implications for Origin, Lithospheric Setting, and Distinction from Other Epigenetic Iron Oxide Deposits. *Econ. Geol.* **2010**, *105*, 641–654. [CrossRef]
4. Roberts, D.E.; Hudson, G.R.T. The Olympic Dam Copper-Uranium-Gold Deposit, Roxby Downs, South Australia. *Econ. Geol.* **1983**, *78*, 799–822. [CrossRef]
5. Oreskes, N.; Einaudi, M.T. Origin of Rare Earth Element-Enriched Hematite Breccias at the Olympic Dan Cu-U-Au-Ag Deposit, Roxby Downs, South Australia. *Econ. Geol.* **1990**, *85*, 1–18. [CrossRef]
6. Lottermoser, B.G. Rare Earth Element Mineralogy of the Olympic Dam Cu-U-Au-Ag Deposit, Roxby Downs, South Australia: Implications for Ore Genesis. *Neues Jahrb. Mineral. Monatshefte* **1995**, *8*, 371–384.
7. Ehrig, K.; McPhie, J.; Kamenetsky, V.S. Geology and mineralogical zonation of the Olympic Dam iron oxide Cu-U-Au-Ag deposit, South Australia. In *Geology and Genesis of Major Copper Deposits and Districts of the World, a Tribute to Richard Sillitoe*; Society of Economic Geologists Special Publication; Hedenquist, J.W., Harris, M., Camus, F., Eds.; SEG: Littleton, CO, USA, 2012; Volume 16, pp. 237–268.
8. Macmillan, E.; Cook, N.J.; Ehrig, K.; Ciobanu, C.L.; Pring, A. Uraninite from the Olympic Dam IOCG-U-Ag deposit: Linking textural and compositional variation to temporal evolution. *Am. Mineral.* **2016**, *101*, 1295–1320. [CrossRef]
9. Macmillan, E.; Cook, N.J.; Ehrig, K.; Pring, A. Chemical and textural interpretation of late stage coffinite and brannerite from the Olympic Dam IOCG-Ag-U deposit. *Mineral. Mag.* **2017**. [CrossRef]
10. Krneta, S.; Ciobanu, C.L.; Cook, N.J.; Ehrig, K.; Kontonikas-Charos, A. Apatite at Olympic Dam, South Australia: A petrogenetic tool. *Lithos* **2016**, *262*, 470–485. [CrossRef]
11. Krneta, S.; Ciobanu, C.L.; Cook, N.J.; Ehrig, K.; Kontonikas-Charos, A. Rare earth element behaviour in apatite from the Olympic Dam Cu-U-Au-Ag deposit, South Australia. *Minerals* **2017**, *7*, 135. [CrossRef]
12. Kontonikas-Charos, A.; Ciobanu, C.L.; Cook, N.J.; Ehrig, K.; Krneta, S.; Kamenetsky, V.S. Feldspar Evolution in the Roxby Downs Granite, Host to Fe-Oxide Cu-Au-(U) Mineralisation at Olympic Dam, South Australia. *Ore Geol. Rev.* **2017**, *80*, 838–859. [CrossRef]
13. Kontonikas-Charos, A.; Ciobanu, C.L.; Cook, N.J.; Ehrig, K.; Ismail, R.; Krneta, S.; Basak, A. Feldspar mineralogy and rare earth element (re)mobilization in iron-oxide copper gold systems from South Australia: A nanoscale study. *Mineral. Mag.* **2017**. [CrossRef]
14. Donnay, G.; Donnay, J.D.H. The crystallography of bastnaesite, parisite, roentgenite and synchysite. *Am. Mineral.* **1953**, *38*, 932–963.
15. Van Landuyt, J.; Amelinckx, S. Multiple Beam Direct Lattice Imaging of New Mixed-Layer Compounds of the Bastnaesite-Synchisite Series. *Am. Mineral.* **1975**, *60*, 351–358.

16. Ni, Y.; Hughes, J.M.; Mariano, A.N. The Atomic Arrangement of Bastnäsite-(Ce), $Ce(CO_3)F$, and Structural Elements of Synchysite-(Ce), Rontgenite-(Ce), and Parisite-(Ce). *Am. Mineral.* **1993**, *78*, 415–418.
17. Wu, X.; Dawei, M.; Zhaolu, P.; Guangming, Y. Transmission Electron Microscopic Study of New, Regular, Mixed-Layer Structures in Calcium-Rare-Earth Fluorocarbonate Minerals. *Mineral. Mag.* **1998**, *62*, 55–64.
18. Meng, D.; Wu, X.; Han, Y.; Meng, X. Polytypism and microstructures of the mixed-layer member B_2S, $CaCe_3(CO_3)_4F_3$ in the bastnaesite-(Ce)-synchysite-(Ce) series. *Earth Planet. Sci. Lett.* **2002**, *203*, 817–828. [CrossRef]
19. Wang, L.; Ni, Y.; Hughes, J.M.; Bayliss, P.; Drexler, J.W. The atomic arrangement of synchysite-(Ce), $CeCaF(CO_3)_2$. *Can. Mineral.* **1994**, *32*, 865–871.
20. Ni, Y.; Post, J.E.; Hughes, J.M. The Crystal Structure of Parisite-(Ce), $Ce_2CaF_2(CO_3)_3$. *Am. Mineral.* **2000**, *85*, 251–258. [CrossRef]
21. Williams-Jones, A.E.; Wood, S.A. A preliminary petrogenetic grid for REE fluorocarbonates and associated minerals. *Geochim. Cosmochim. Acta* **1992**, *56*, 725–738. [CrossRef]
22. Gysi, A.P.; Williams-Jones, A.E. The Thermodynamic Properties of Bastnäsite-(Ce) and Parisite-(Ce). *Chem. Geol.* **2015**, *392*, 87–101. [CrossRef]
23. Yang, H.; Dembowski, R.F.; Conrad, P.G.; Downs, R.T. Crystal Structure and Raman Spectrum of Hydroxyl-Bästnasite-(Ce), $CeCO_3(OH)$. *Am. Mineral.* **2008**, *93*, 698–701. [CrossRef]
24. Hsu, L.C. Synthesis and Stability of Bastnaesites in a Part of the System (Ce,La)-F-H-C-O. *Mineral. Petrol.* **1992**, *47*, 87–101. [CrossRef]
25. Shivaramaiah, R.; Anderko, A.; Riman, R.E.; Navrotsky, A. Thermodynamics of Bastnaesite: A Major Rare Earth Ore Mineral. *Am. Mineral.* **2016**, *101*, 1129–1134. [CrossRef]
26. Holtstam, D.; Grins, J.; Nysten, P. Haleniusite-(La) from the Bastnäs deposit, Västmanland, Sweden: A new REE Oxyfluoride mineral species. *Can. Mineral.* **2004**, *42*, 1097–1103. [CrossRef]
27. Allen, S.R.; McPhie, J.; Ferris, G.; Simpson, C. Evolution and Architecture of a Large Felsic Igneous Province in Western Laurentia: The 1.6 Ga Gawler Range Volcanics, South Australia. *J. Volcanol. Geotherm. Res.* **2008**, *172*, 132–147. [CrossRef]
28. Johnson, J.P.; Cross, K.C. U-Pb geochronological constraints on the genesis of the Olympic Dam Cu-U-Au-Ag deposit, South Australia. *Econ. Geol.* **1995**, *90*, 1046–1063. [CrossRef]
29. Creaser, R.A.; Cooper, J.A. U-Pb Geochronology of Middle Proterozoic Felsic Magmatism Surrounding the Olympic Dam Cu-U-Au-Ag and Moonta Cu-Au-Ag Deposits, South Australia. *Geology* **1993**, *88*, 186–197. [CrossRef]
30. Ciobanu, C.L.; Wade, B.; Cook, N.J.; Schmidt Mumm, A.; Giles, D. Uranium-bearing hematite from the Olympic Dam Cu-U-Au deposit, South Australia; a geochemical tracer and reconnaissance Pb-Pb geochronometer. *Precambrian Res.* **2013**, *238*, 129–147. [CrossRef]
31. Courtney-Davies, L.; Zhu, Z.; Ciobanu, C.L.; Wade, B.P.; Cook, N.J.; Ehrig, K.; Cabral, A.R.; Kennedy, A. Matrix-matched iron-oxide laser ablation ICP-MS U-Pb geochronology using mixed solutions standards. *Minerals* **2016**, *6*, 85. [CrossRef]
32. Apukhtina, O.B. Distribution, Petrology, Geochemistry and Geochronology of Carbonate Assemblages at the Olympic Dam Deposit. Ph.D. Thesis, University of Tasmania, Hobart, Australia, 2016.
33. Ciobanu, C.L.; Kontonikas-Charos, A.; Slattery, A.; Cook, N.J.; Ehrig, K.; Wade, B.P. Short-range stacking disorder inmixed layer compounds A HAADF STEM study of bastnäsite-parisite intergrowths. *Minerals* **2017**. under review.
34. Diemar, G.A. The Petrology of Hydrothermal Rare Earth Element Bearing Minerals in the Olympic Dam IOCG Deposit Support a 1.3 Ga formation. MSc Thesis, University of Tasmania, Hobart, Australia, 2014.
35. Smith, M.P.; Henderson, P.; Campbell, L.S. Fractionation of the REE during Hydrothermal Processes: Constraints from the Bayan Obo Fe-REE-Nb Deposit, Inner Mongolia, China. *Geochim. Cosmochim. Acta* **2000**, *64*, 3141–3160. [CrossRef]
36. McDonough, W.F.; Sun, S.-S. Composition of the Earth. *Chem. Geol.* **1995**, *120*, 223–253. [CrossRef]
37. Fleischer, M. Relative proportions of the lanthanides in minerals of the bastnaesite group. *Can. Mineral.* **1978**, *16*, 361–363.
38. Holtstam, D.; Andersson, U.B. The REE minerals of the Bastnäs-type deposits, South-Central Sweden. *Can. Mineral.* **2007**, *45*, 1073–1114. [CrossRef]

39. Forster, H.J. Cerite-(Ce) and thorian synchysite-(Ce) from the Niederbobritzsch Granite, Erzgebirge, Germany: Implications for the differential mobility of the LREE and Th during alteration. *Can. Mineral.* **2000**, *38*, 67–79. [CrossRef]
40. Grammatikopoulos, T.; Mercer, W.; Gunning, C.; Prout, S. Quantitative characterization of the REE minerals by QEMSCAN from the Nechalacho Heavy Rare Earth Deposit, Thor Lake Project, NWT, Canada. *SGS Miner. Serv. Tech. Pap.* **2011**, *7*, 1–11.
41. Papoutsa, A.; Pe-Piper, G. Variation of REE-Hydrothermal Circulation in Complex Shear Zones: The Cobequid Highlands, Nova Scotia. *Can. Mineral.* **2014**, *52*, 943–968. [CrossRef]
42. Zaitsev, A.N.; Wall, F.; Le Bas, M.J. REE-Sr-Ba minerals from the Khibina Carbonatites, Kola Peninsula, Russia: Their mineralogy, paragenesis and evolution. *Mineral. Mag.* **1998**, *62*, 225–250. [CrossRef]
43. Broom-Fendley, S.; Brady, A.E.; Wall, F.; Gunn, G.; Dawes, W. REE Minerals at the Songwe Hill Carbonatite, Malawi: HREE-Enrichment in Late-Stage Apatite. *Ore Geol. Rev.* **2017**, *81*, 23–41. [CrossRef]
44. Guastoni, A.; Nestola, F.; Giaretta, A. Mineral Chemistry and Alteration of Rare Earth Element (REE) Carbonates from Alkaline Pegmatites of Mount Malosa, Malawi. *Am. Mineral.* **2009**, *94*, 1216–1222. [CrossRef]
45. Augé, T.; Bailly, L.; Wille, G. An Unusual Occurrence of Synchysite-(Ce) in Amygdules from the Esterel Volcanic Rocks, France: Implications for Rare-Earth Element Mobility. *Can. Mineral.* **2014**, *52*, 1–19. [CrossRef]
46. Mondillo, N.; Boni, M.; Balassone, G.; Spoleto, S.; Stellato, F.; Marino, A.; Santoro, L.; Spratt, J. Rare Earth Elements (REE)—Minerals in the Silius Fluorite Vein System (Sardinia, Italy). *Ore Geol. Rev.* **2016**, *74*, 211–224. [CrossRef]
47. Vasyukova, O.; Williams-Jones, A.E. The Evolution of Immiscible Silicate and Fluoride Melts: Implications for REE Ore-Genesis. *Geochim. Cosmochim. Acta* **2016**, *172*, 205–224. [CrossRef]
48. Savko, K.A.; Bazikov, N.S. Phase Equilibria of Bastnaesite, Allanite, and Monazite: Bastnaesite-out Isograde in Metapelites of the Vorontsovskaya Group, Voronezh Crystalline Massif. *Petrology* **2011**, *19*, 445–469. [CrossRef]
49. Groves, D.I.; Vielreicher, N.M. The Phalabowra (Palabora) carbonatite-hosted magnetite-copper sulfide deposit, South Africa: An end-member of the iron-oxide copper-gold-rare earth element deposit group? *Miner. Depos.* **2001**, *36*, 189–194. [CrossRef]
50. Bau, M. Controls on the Fractionation of Isovalent Trace Elements in Magmatic and Aqueous Systems: Evidence from Y/Ho, Zr/Hf, and lanthanide tetrad effect. *Contrib. Mineral. Petrol.* **1996**, *123*, 323–333. [CrossRef]
51. Tanaka, K.; Takahashi, Y.; Shimizu, H. Local structure of Y and Ho in calcite and its relevance to Y fractionation from Ho in partitioning between calcite and aqueous solution. *Chem. Geol.* **2008**, *248*, 104–113. [CrossRef]
52. Brugger, J.; Liu, W.; Etschmann, B.; Mei, Y.; Sherman, D.M.; Testemale, D. A Review of the Coordination Chemistry of Hydrothermal Systems, or Do Coordination Changes Make Ore Deposits? *Chem. Geol.* **2016**, *447*, 219–253. [CrossRef]
53. Williams-Jones, A.E.; Migdisov, A.A.; Samson, I.M. Hydrothermal Mobilisation of the Rare Earth Elements—A Tale of 'Ceria' and 'Yttria'. *Elements* **2012**, *8*, 355–360. [CrossRef]
54. McPhie, J.; Kamenetsky, V.; Allen, S.; Ehrig, K.; Agangi, A.; Bath, A. The fluorine link between a supergiant ore deposit and silicic large igneous province. *Geology* **2011**, *39*, 1003–1006. [CrossRef]
55. Haas, J.R.; Shock, E.L.; Sassani, D.C. Rare Earth Elements in Hydrothermal Systems: Estimates of Standard Partial Molal Thermodynamic Properties of Aqueous Complexes of the Rare Earth Elements at High Pressures and Temperatures. *Geochem. Explor. Environ. Anal.* **1995**, *59*, 4329–4350. [CrossRef]
56. Didier, A.; Bosse, V.; Boulvais, P.; Bouloton, J.; Paquette, J.-L.; Montel, J.-M.; Devidal, J.-L. Disturbance versus preservation of U-Th-Pb ages in monazite during fluid-rock interaction: Textural, chemical and isotopic in situ study in microgranites (Velay Dome, France). *Contrib. Mineral. Petrol.* **2013**, *165*, 1051–1072. [CrossRef]

© 2017 by the authors. Licensee MDPI, Basel, Switzerland. This article is an open access article distributed under the terms and conditions of the Creative Commons Attribution (CC BY) license (http://creativecommons.org/licenses/by/4.0/).